Icarus 303 (2018) 22–33

Contents lists available at ScienceDirect

Icarus

journal homepage: www.elsevier.com/locate/icarus

Population characteristics of submicrometer-sized craters on regolith particles from asteroid Itokawa

Toru Matsumoto[a,*], S. Hasegawa[a], S. Nakao[b], M. Sakai[b], H. Yurimoto[a,c]

[a] Institute of Space and Astronautical Science, Japan Aerospace Exploration Agency, 3-1-1, Yoshinodai, Chuo-ku, Sagamihara, Kanagawa 252-5210, Japan
[b] Institute for Molecular Science, 38 Nishigo-Naka, Myodaiji, Okazaki 444-8585, Japan
[c] Natural History Sciences, Hokkaido University, Kita-10 Nishi-8 Kita-ku, Sapporo 060-0810, Japan

ARTICLE INFO

Article history:
Received 20 September 2017
Revised 7 December 2017
Accepted 11 December 2017
Available online 16 December 2017

ABSTRACT

We investigated impact crater structures on regolith particles from asteroid Itokawa using scanning electron microscopy. We observed the surfaces of 51 Itokawa particles, ranging from 15 μm to 240 μm in size. Craters with average diameters ranging from 10 nm to 2.8 μm were identified on 13 Itokawa particles larger than 80 μm. We examined the abundance, spatial distribution, and morphology of approximately 900 craters on six Itokawa particles. Craters with sizes in excess of 200 nm are widely dispersed, with spatial densities from 2.6 μm^2 to 4.5 μm^2; a fraction of the craters was locally concentrated with a density of 0.1 μm^2. The fractal dimension of the cumulative crater diameters ranges from 1.3 to 2.3. Craters of several tens of nanometers in diameter exhibit pit and surrounding rim structures. Craters of more than 100 nm in diameter commonly have melted residue at their bottom. These morphologies are similar to those of submicrometer-sized craters on lunar regolith. We estimated the impactor flux on Itokawa regolith-forming craters, assuming that the craters were accumulated during direct exposure to the space environment for 10^2 to 10^4 yr. The range of impactor flux onto Itokawa particles is estimated to be at least one order of magnitude higher than the interplanetary dust flux and comparable to the secondary impact flux on the Moon. This indicates that secondary ejecta impacts are probably the dominant cratering process in the submicrometer range on Itokawa regolith particles, as well as on the lunar surface. We demonstrate that secondary submicrometer craters can be produced anywhere in centimeter- to meter-sized depressions on Itokawa's surface through primary interplanetary dust impacts. If the surface unevenness on centimeter to meter scales is a significant factor determining the abundance of submicrometer secondary cratering, the secondary impact flux could be independent of the overall shapes or sizes of celestial bodies, and the secondary impact flux could have similar values on Itokawa and the Moon.

1. Introduction

Solar system objects without atmospheres are continuously exposed to hypervelocity impacts. Impact processes are considered to be among the fundamental agents causing the modification of surface geological features of airless bodies. They include impact cratering (e.g., Melosh, 1989), regolith formation (e.g., Melosh, 1989), regolith mixing, and migration (e.g., Robinson et al., 2001; Veverka et al., 2001; Miyamoto et al., 2007). In addition, microscopic meteoroid impacts contribute to changes in the optical properties, chemical composition, and structures of regolith surface material through impact melting, vaporization, and condensation processes, so-called 'space weathering' (e.g., Clark et al., 2002). Surface evolution caused by hypervelocity impacts can offer important clues to understanding the history of airless bodies in the solar system.

The Hayabusa spacecraft touched down on an S-type near-Earth asteroid, 25,143 Itokawa (Yano et al., 2006), and recovered regolith particles from its surface (Yada et al., 2014). Mineralogical and oxygen isotope properties of Itokawa particles are consistent with those of LL5–6 chondrite (Nakamura et al., 2011; Tsuchiyama et al., 2011; Yurimoto et al., 2011; Nakashima et al., 2013). Itokawa particles contain solar-wind gases and cosmogenic nuclei, implying that they remained on the asteroid's surface (Nagao et al., 2011). Partially crystalline rims containing nanoparticles provide evidence of space weathering effects on S-type asteroids, where solar-wind irradiation damage and implantation are the major causes of rim formation, whereas micrometeoroid impacts play only a minor role

* Corresponding author.
E-mail address: tmatsumoto@planeta.sci.isas.jaxa.jp (T. Matsumoto).

https://doi.org/10.1016/j.icarus.2017.12.017

(Noguchi et al., 2011; Harries and Langenhorst, 2014; Keller and Berger, 2014; Noguchi et al., 2014; Thompson et al., 2014; Bonal et al., 2015; Matsumoto et al., 2015; Harries et al., 2016; Matsumoto et al., 2016). In addition, regolith activity on Itokawa—probably driven by impact processes—has been identified based on grain motion (Nagao et al., 2011; Matsumoto et al., 2016), fracturing (Tsuchiyama et al., 2011; Langenhorst et al., 2014; Matsumoto et al., 2016), and abrasion (Tsuchiyama et al., 2011). These previous studies have shown that Itokawa particles contain a record of the collective processes of regolith evolution on this small asteroid.

In previous studies, submicrometer-sized impact craters have been found on Itokawa particles (Nakamura et al., 2012; Harries et al., 2016; Matsumoto et al., 2016). These natural, small-scale craters can offer insights into the process of small-scale hypervelocity impacts, for which impact experiments in the laboratory have not yet yielded a comprehensive picture. In addition, these small craters can provide information about the unknown origin of the micrometeoroids bombarding Itokawa and the possible contribution to space weathering by submicrometer impacts (Harries et al., 2016). Craters with diameters from micrometers to a few tens of nanometers are generally observed on lunar regolith (e.g., Brownlee et al., 1973; Schneider et al., 1973; Fechtig et al., 1974; Morrison and Zinner, 1977; Morrison and Clanton, 1979), as well as on the meteoritic regolith breccias Kapoeta (howardite; Brownlee and Rajan, 1973) and Murchison (CM2 chondrite; Goswami et al., 1976). Therefore, understanding submicrometer-sized cratering processes on Itokawa particles can contribute to a general interpretation of small-scale impacting processes on airless bodies.

Previous studies have reported that the abundance of submicrometer craters on Itokawa particles is very low compared with similar features on lunar regolith; detailed surface observations identified only 24 submicrometer craters on 32 Itokawa particles with sizes from 20 μm to 50 μm (Nakamura et al., 2012; Harries et al., 2016; Matsumoto et al., 2016). Nakamura et al. (2012) suggested that submicrometer craters can be formed through direct impacts of nanometer-sized interplanetary dust particles. In contrast, the submicrometer craters found on Itokawa particles may have formed through impacts of secondary ejecta created by primary impacts on Itokawa, because submicrometer craters appear to be concentrated on only a limited number of specific Itokawa particles (Harries et al., 2016; Matsumoto et al., 2016). So far, statistical analysis of these craters has been limited because of the low crater abundances observed. Therefore, it is not clear whether the few observed craters represent the whole evolutionary picture of submicrometer cratering processes on Itokawa. In addition, the detailed abundances and production rates of submicrometer caters are not understood.

At the Extraterrestrial Sample Curation Center of the Japan Aerospace Exploration Agency (JAXA), Itokawa particles with an average diameter of 30 μm were retrieved from a sample catcher in the Hayabusa sample container (Yada et al., 2014). Thus far, surface features of Itokawa particles larger than 100 μm have never been examined in detail. These large Itokawa particles have large surface areas and they are the most suitable particles for extensive investigations of impact craters. The objective of the present work is to reveal accurate abundances of submicrometer craters and determine whether secondary impacts are representative agents driving the small-scale cratering processes on Itokawa. In the present study, we performed surface observations of 51 Itokawa particles ranging in size from approximately 15 μm to 240 μm and obtained unprecedented information on the areal distributions and morphologies of the craters on Itokawa particles. We report approximately 900 craters on Itokawa particles and compare the crater population with the flux of interplanetary dust particles and the lunar dust environment.

2. Observations

2.1. Samples

The Itokawa particles investigated in this study are listed in Table 1. The listed particles were collected from rooms A and B of a sample catcher, captured during the second and first touchdowns in the MUSES-C Region of Itokawa, respectively (Yada et al., 2014). The particles from room A (ID: RA-QD02-XXXX) were retrieved from a pure quartz disk after gently tapping on the exterior of the sample catcher, causing particles to drop onto the pure quartz disk (Yada et al., 2014). The particles from room B (ID: RB-CV-XXXX) analyzed in the present study were retrieved from the cover of room B (Yada et al., 2014). We examined 29 particles from room A (average diameters 24–240 μm) and 22 particles from Room B (average diameters 15–50 μm). The mineral phases and average diameters of the Itokawa particles (Table 1) were investigated based on their initial description (the detailed database is available at http://hayabusaao.isas.jaxa.jp/curation/hayabusa/index.html).

2.2. Observational procedure

Itokawa particles retrieved from the quartz disk and cover of room B were first analyzed with the field emission scanning electron microscope (FE-SEM; Hitachi SU6600) at the JAXA curation center to enable an initial description and preliminary identification of particle size and major mineral phases (Yada et al., 2014). The particles were placed on a gold-coated holder using an electrostatically controlled micromanipulation system.

In this study, we observed the surface morphologies of Itokawa particles using the FE-SEM after the routine initial description procedure. The particles were observed without conductive coating. As described by Yada et al. (2014), Itokawa particles observed in this study have never been exposed to an atmospheric environment, thus suppressing contamination and alteration of the particles. We performed secondary electron (SE) image observation at accelerating voltages of 1.5 kV and/or 2 kV in high vacuum with an electron beam current of approximately 10 pA. To assess their surface concavity or convexity, Itokawa particles were imaged from two angles, with a difference in tilt of 5°, to create stereograms. The particle surfaces were scanned initially at magnifications of 2000–10,000 in order to identify the presence of craters. Surfaces containing craters were re-examined at magnifications of up to 150,000.

One crater-rich Itokawa particle (RA-QD02-0275) was allocated for further research as part of JAXA's quota. The particle was adhered onto a carbon-conductive tape to secure sufficient electrical conduction for SEM analysis. This sample handling procedure was performed in a nitrogen-filled glove box at the JAXA curation center. Next, we transferred the particle to the Institute for Molecular Science (IMS, Higashi-okazaki, Japan). The particle was stored in a vacuum desiccator during transportation. We determined the elemental composition of its surface through energy-dispersive X-ray spectroscopy (EDS) using an FE-SEM (Hitachi SU6600) equipped with a Bluker XFlash® FlatQUAD detector at the IMS. The accelerating voltage for SE imaging was 1.5 kV, while for EDS analysis we used 5 kV and 10 kV.

3. Results

3.1. Spatial crater distribution

We identified numerous submicrometer-sized craters (Figs. 1 and 2) on 13 of the 29 Itokawa particles from room A (Fig. 3). On the other hand, we did not identify craters on Itokawa particles obtained from the cover of room B. The size distribution of

Table 1
Itokawa particles investigated in this study.

ID	Mineral phase[a]	Diameter (μm)[b]	Surface type	Surface features		
				Crater	Melt drop/splash	Blister
RA-QD02-0271	ol,pl,FeNi	130	F	nf	nf	nf
RA-QD02-0272	ol,lpx,hpx,tr	137	F	a	a	a
RA-QD02-0273	ol,hpx,K-feld	204	F/D	a	a	a
RA-QD02-0274	hpx,ol,lpx,pl	148	F	nf	nf	p
RA-QD02-0275	ol	122	F	a	a	a
RA-QD02-0276	ol,hpx,ap,lpx,pl,tr	84	F	nf	nf	nf
RA-QD02-0277	hpx,lpx,ol,pl,tr.chm	171	F	a	a	a
RA-QD02-0278	ol	84	F	a	a	a
RA-QD02-0279	ol,pl	143	F	p	p	p
RA-QD02-0280	ol,tr	86	F	nf	nf	nf
RA-QD02-0281	ol,chm	80	F	nf	nf	nf
RA-QD02-0282	ol,chm	241	F	nf	a	a
RA-QD02-0283	ol	121	D/F	a	a	a
RA-QD02-0285	ol,chm	105	F	nf	nf	nf
RA-QD02-0286	pl,ol,hpx,tr	168	F	a	a	a
RA-QD02-0287	ol,hpx,pl	99	D	nf	nf	a
RA-QD02-0288	hpx,pl,lpx	156	F	nf	nf	nf
RA-QD02-0290	pl,ol,FeNi	53	D	nf	a	a
RA-QD02-0291	ol	88	F	nf	nf	p
RA-QD02-0292	ol, pl,lpx,tr	78	F	nf	p	a
RA-QD02-0294	ol	24	F	nf	nf	a
RA-QD02-0295	tr,pl	35	F	nf	nf	nf
RA-QD02-0296	pl,tr	68	D/F	nf	nf	nf
RA-QD02-0297	ol,FeNi,chm	115	F	a	a	a
RA-QD02-0301	tr,pl,ol	213	F	a	a	a
RA-QD02-0302	tr,lpx	105	F	nf	nf	nf
RA-QD02-0305	ol	241	F	p	p	p
RA-QD02-0306	pl,ol,lpx,chm	134	F	a	a	a
RA-QD02-0307	ol,lpx	92	D/F	a	a	a
RB-CV-0267	ol	29	D	nf	a	a
RB-CV-0268	pl	21	F	nf	nf	nf
RB-CV-0269	pl	16	F	nf	nf	nf
RB-CV-0270	lpx	16	F	nf	nf	nf
RB-CV-0271	ol	16	F	nf	nf	nf
RB-CV-0272	lpx, ol	16	F	nf	nf	nf
RB-CV-0273	ol	15	F	nf	nf	nf
RB-CV-0275	pl,ol	15	F/D	nf	a	nf
RB-CV-0279	lpx	16	F	nf	nf	nf
RB-CV-0280	ol	15	F	nf	nf	nf
RB-CV-0281	lpx	26	F	nf	nf	nf
RB-CV-0282	lpx	32	F	nf	nf	nf
RB-CV-0283	lpx,pl	46	F	nf	nf	nf
RB-CV-0284	pl	18	F	nf	nf	nf
RB-CV-0285	lpx	16	F	nf	nf	nf
RB-CV-0286	ol	18	F	nf	a	a
RB-CV-0287	pl,ol	21	F	nf	a	a
RB-CV-0289	hpx,pl	17	F	nf	a	a
RB-CV-0290	hpx	15	F	nf	a	a
RB-CV-0291	hpx	20	F	nf	a	a
RB-CV-0292	hpx	20	F	nf	a	a
RB-CV-0296	lpx,hpx	15	F	nf	nf	p

Notes: F = fractured surface; D = surface of micro druse;; a = abundant; a* = ; p = poor; nf = not found. [a] Mineral phases identified on grain surfaces by SEM observation.ol: olivine; hpx: high-Ca pyroxene; lpx: low-Ca pyroxene; pl: plagioclase; K-feld: potassium-dominant feldspars; tr: troilite; FeNi: iron-nickel metal; chm: chromite; ap: apatite. [b] Average values of long and short axes of Itokawa particles measured from SEM observation. The mineral phase and size of particles in this table are reported in detail in the Hayabusa sample list database (http://hayabusaao.isas.jaxa.jp).

Itokawa particles observed here is shown in Fig. 3. In the present study, all Itokawa particles on which craters were found are larger than 80 μm. In contrast, craters were not identified on Itokawa particles smaller than 80 μm. Detailed SEM observations showed that 11 of the 13 Itokawa particles containing craters had more than 30 craters on their surfaces (henceforth referred to as 'crater-rich' particles). The other two particles (RA-QD02-0279 and RA-QD02-0305) contain few craters. On 8 of the 11 crater-rich particles, the craters are widely dispersed across the particle surfaces, as shown in Fig. 4A. However, craters tend to concentrate locally on two of the 11 crater-rich particles (RA-QD02-0273, RA-QD02-0277: Fig. 4B). One of the 11 crater-rich particles is an assemblage of small, fractured fragments (RA-QD02-0272). The crater density on RA-QD02-0272 varies between the fragments, and the craters are particularly concentrated on a specific fragment (Fig. 1).

The front and rear faces of several Itokawa particles were observed when they were turned over during the SEM observations. The distribution of craters on the different surfaces of individual Itokawa particles differed among particles: Craters were widely distributed on the opposite and side surfaces of RA-QD02-0275, similarly to its front surface (Fig. 4A), while there are few craters on the RA-QD02-0273 surface opposite to the front surface (Fig. 4B).

The surfaces of Itokawa particles can be divided into two types on the basis of their formation processes (Matsumoto et al., 2016). One type is a fractured surface (Fig. 4A), which is formed by im-

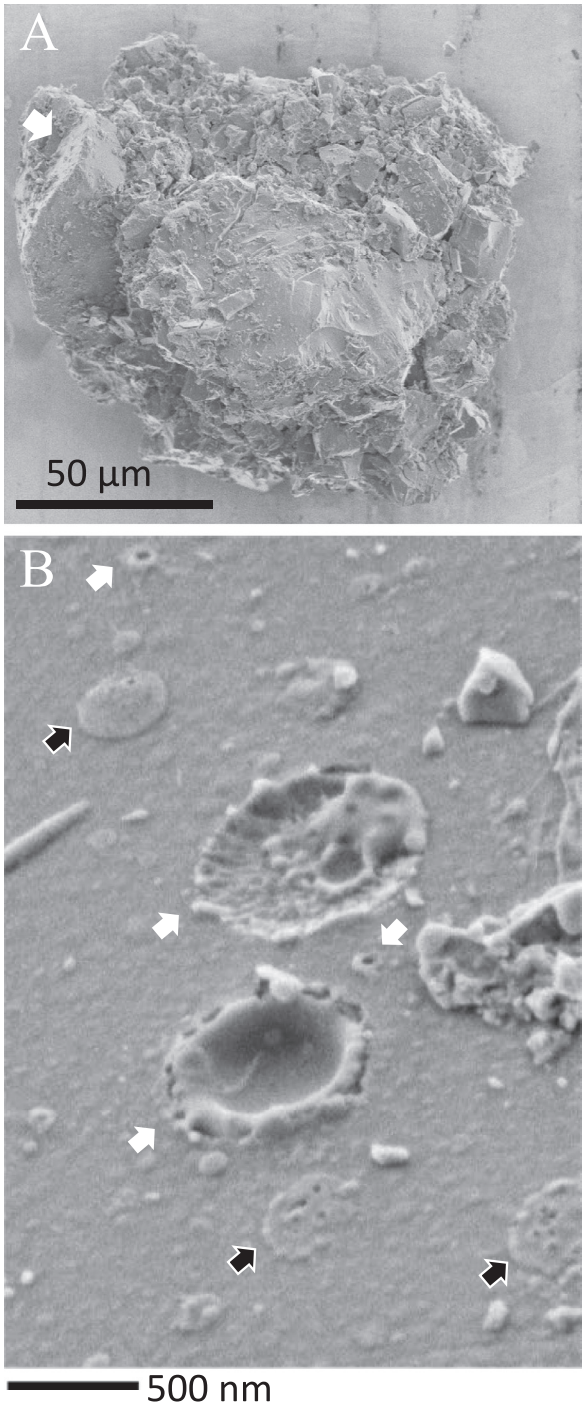

Fig. 1. (A) Secondary electron (SE) image of RA-QD02-0272. The white arrow shows a crater-rich olivine fragment. (B) SE image of craters on the crater-rich fragment indicated in panel (A). This surface was imaged from an oblique angle. Craters and melt droplets are indicated by white and black arrows, respectively. Blisters commonly appear in the field of view.

pacts and/or possibly thermal fatigue. Another type is a surface with concentric polygonal steps and/or euhedral grains (Fig. 4B), which is thought to have formed through thermal annealing in pores on Itokawa's parent body. Pores with euhedral–subhedral crystals are often observed in porous ordinary chondrites and were termed 'micro-druses' by Matsumoto et al. (2016). In the present study, the surfaces of Itokawa particles can be also classified as belonging to one of these two types (Table 1). Craters can be identified regardless of the two surface types.

3.2. Crater morphology

Typical submicrometer craters on Itokawa particles observed in this study are shown in Figs. 1 and 2. Craters from several tens to 100 nm in diameter are characterized by a pit and a surrounding rim (Fig. 2A). Craters larger than 200 nm in diameter are frequently covered with melted material from the bottom to the rim of the craters (Figs. 1B and 2B, C). These morphologies are similar to those of submicrometer craters on both lunar rocks (Morrison and Clanton, 1979) and fragments of Murchison carbonaceous chondrites (Goswami et al., 1976). These melted materials occasionally flow radially over the edge of the craters (Fig. 1B; Fig. 8B of Matsumoto et al., 2016). Occasionally, craters exhibit highly elongated outlines, as shown in Fig. 2D. As regards craters on troilite grains, cracks appear at their bottom, which are not observed in craters on silicate grains (Fig. 2E). The largest crater found in this study has an average size of 2.8 μm. It consists of an irregularly shaped melted object with concave features. Convex, fine spotted structures of 10–100 nm in size are frequently distributed on surfaces containing craters (Figs. 1B and 2B–F). The spotted structures are probably blisters, which are thought to have formed through accumulation of solar-wind-entrained hydrogen and helium implanted within 60–80 nm (Noguchi et al., 2014; Matsumoto et al., 2015). The blisters might have developed through solar wind irradiation within the order of 10^3 years (Noguchi et al., 2014). In many cases, craters are devoid of blisters on their surfaces, although blisters may have developed near them (Fig. 2B, F). Occasionally, blisters appear at the bottom of the craters (Fig. 2C–E). Melt drops and melt splashes are generally observed on surfaces with craters (Fig. 1B). Craters in Fig. 2B–D are dispersed on the same particle surface as in Fig. 4A; craters with or without blisters and elongated craters coexist on the same surfaces. Enlarged images of locally concentrated craters (Fig. 4B) correspond to Fig. 2A. Rims of concentrated craters tend to disappear in the same direction (upper parts of the crater rims disappear in Fig. 2A).

3.3. Crater size distribution

We measured the cumulative number of craters on Itokawa particles as a function of crater diameter (Fig. 5). Six Itokawa particles with abundant craters were selected. They consist of particles characterized by different minerals, surface types (fractured or micro-druse surfaces), and crater distributions (widely dispersed or locally concentrated), as summarized in Table 2. Regarding the observation of RA-QD02-0273 and RA-QD02-0278, some craters might have been overlooked because these surfaces were not scanned at the same magnification as RA-QD02-0275, RA-QD02-0283, RA-QD02-0286, and RA-QD02-0301 (Table 2). Crater diameters were defined as the distance from the top of the crater rim to the top of the diametrically opposite crater rim. Crater diameters were estimated as the average values of the major and minor axes. Long axes were used as representative crater diameters when craters were observed under oblique angles. In this study, we identified craters ranging from approximately 10 nm to 2.8 μm in diameter. As craters become smaller, it becomes more difficult to identify them unless they have distinct rims. In particular, few craters with sizes of tens of nanometers have been identified if blisters had developed extensively in their vicinity. The obscuration of crater features by blister development can lead to incomplete crater counts and may cause a decrease in the slopes in Fig. 5 below a crater size of 80 nm. Power-law fits to the slopes for craters larger than 80 nm are considered representative slopes of the size distribution. The presence of one or more large craters affects the best-fitting slopes considerably (Harries et al., 2016). Therefore, the largest crater on each particle was excluded for the purpose of our fits. Impact experiments have generally shown that the number of impact frag-

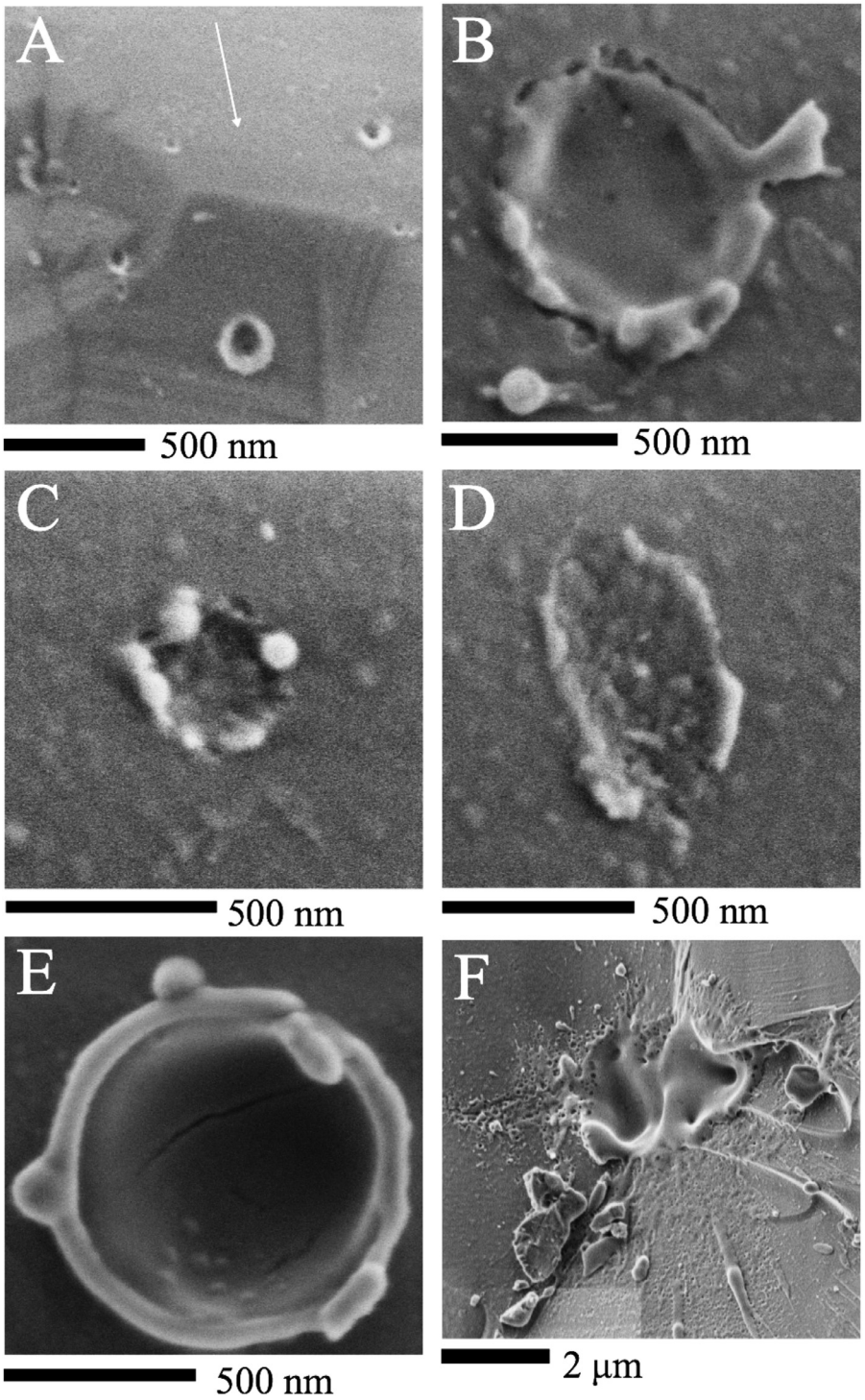

Fig. 2. SE images of typical craters with various diameters on Itokawa particles. (A) Craters ranging from 20 nm to 165 nm in diameter on RA-QD02-0273. The possible impactor trajectory is shown by the arrow, also corresponding to the arrow in Fig. 4B. This image corresponds to an area where craters are locally concentrated, see Fig. 4B. (B)(C) Typical craters larger than 200 nm in diameter on the olivine surface of RA-QD02-0275, see Fig. 4A. (D) Elongated crater on the olivine surface of RA-QD02-0275, see Fig. 4A. (E) Crater on a troilite grain on RA-QD02-0301. A crack appears at the bottom of the crater. (F) The largest crater found in the present study in the olivine surface of RA-QD02-0286.

ments larger than r behaves as $N(r) \propto r^{-D}$, where the exponent D, usually called the fractal dimension, is found to lie in the range $D \in [2, 3]$ (Turcotte, 1986; and references therein). The D values of craters on the six Itokawa particles (Fig. 5A–F) range from $D = 1.3$–2.3. The cumulative number of all craters on the six Itokawa particles (Fig. 5G) is characterized by $D = 2.2$, which is within the range of D values of typical impact fragments.

3.4. Elemental composition

We analyzed elemental maps of 17 craters with sizes from 200 nm to 690 nm on an olivine grain (RAQD02-0275). Fourteen of the 17 craters show no difference in elemental composition from the host olivine grain ($Mg_{1.4}Fe_{0.6}SiO_4$). The EDS spectra of the remaining three craters show Al Kα and Ca Kα peaks. The elemental

Table 2
Itokawa particles observed for investigation of crater size distribution.

ID	Number of craters	Crater distribution*	Magnification**	Investigated area (μm2)	Mineral phase on investigated area***	Surface type****
RA-QD02-0273	266	L		30,802	ol, hpx, K-feld	D
RA-QD02-0275	151	W		8327	ol	FS
RA-QD02-0278	37	W		2873	ol	FS
RA-QD02-0283	128	W		8333	ol	D
RA-QD02-0286	203	W		11,731	pl,ol,hpx,tr	FS
RA-QD02-0301	158	W		4959	tr	FS
Six Itokawa particles	943	–		67,025	–	–

Notes
* Widely dispersed craters (W) or locally concentrated craters (L).
** Magnification used for investigation.
*** ol: olivine; hpx: high-Ca pyroxene; pl: plagioclase; K-feld: potassium-dominant feldspars, tr: troilite.
**** Surface type of investigated area: fractured surface (FS) or surface from micro-druse (D).

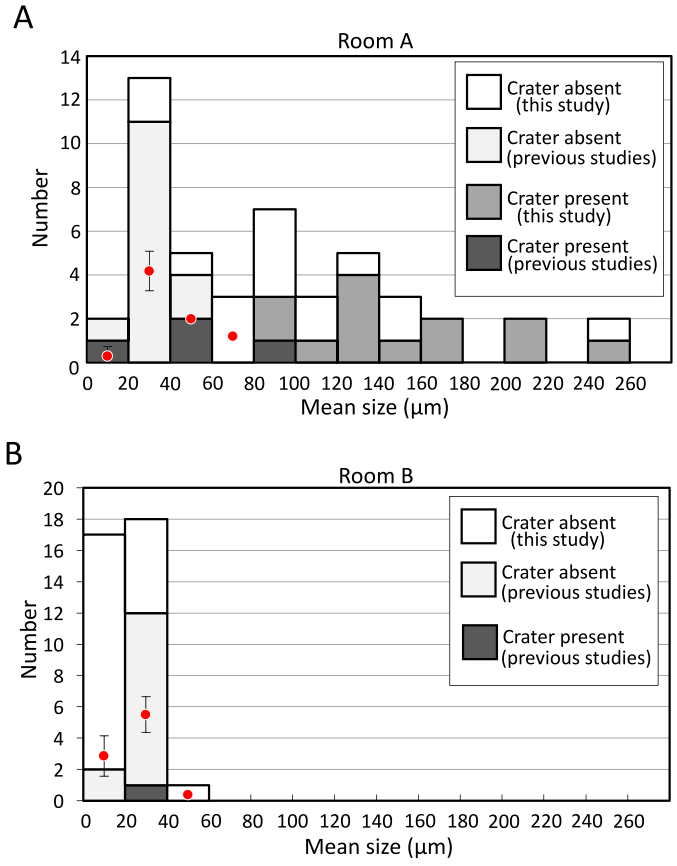

Fig. 3. Size distribution of Itokawa particles from (A) room A and (B) room B observed in the present and in previous studies. Itokawa particles containing craters are labeled as darker gray columns. The size distribution of particles observed in previous studies (Nakamura et al., 2012; Harries et al., 2016; Matsumoto et al., 2016) is also shown. From a re-examination of the SEM data obtained by Matsumoto et al. (2016), two 200-nm-sized crater candidates were found on a 50-μm-sized particle (RA-QD02-0033) on which craters had not been identified previously. This result has been added to Fig. 3. The expected numbers of Itokawa particles containing at least one crater larger than 200 nm, estimated using a crater abundance model for large particles, are plotted as red data points with standard deviations. The standard deviation is too small to display for size bins larger than 40 μm.

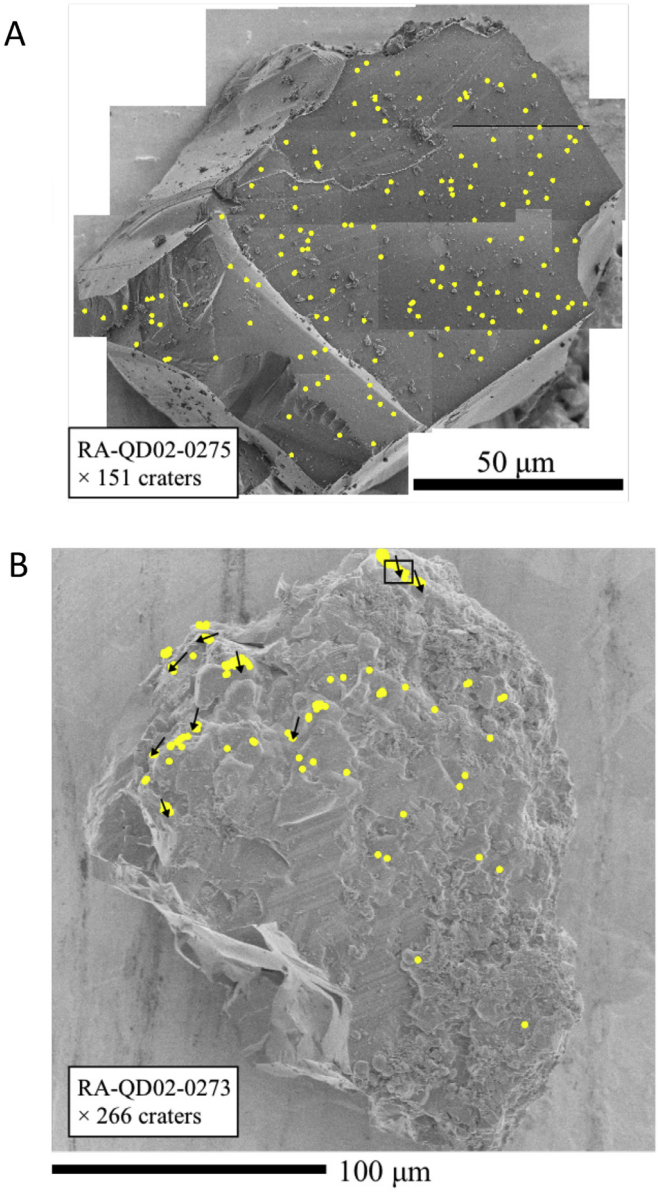

Fig. 4. (A) SE image of an Itokawa olivine particle (RA-QD02-0275). (B) SE image of an Itokawa particle composed of olivine, high Ca pyroxene, and K feldspar (RA-QD02-0273). Yellow dots correspond to the positions of submicrometer-sized craters. In Fig. 4A, 151 craters with diameters ranging from approximately 40 nm to 680 nm are indicated. Close-up images of craters on the particle are shown in Fig. 2B–D. In Fig. 4B, 266 craters with diameters ranging from approximately 10 nm to 440 nm are shown. The majority of the craters are concentrated in the top areas. Fig. 2A corresponds to a close-up image of a concentrated crater area in Fig. 4B (rectangular black area). Possible impactor trajectories are indicated by arrows.

maps of Al Kα and Ca Kα in Fig. 6 show that Al and Ca are distributed from the crater floor to the rim. We also analyzed elemental maps of 12 melted objects (melt splashes and melt droplets) coexisting with craters on RA-QD02-0275. Eleven melted objects show excesses of Na, Al, and Ca, and/or Fe and S with respect to the host olivine surface. Adhering small fragments on the host olivine grain are composed of olivine, pyroxene, plagioclase, FeS, Fe–Ni metals, chromite, and phosphate, which are the major mineral components of Itokawa particles.

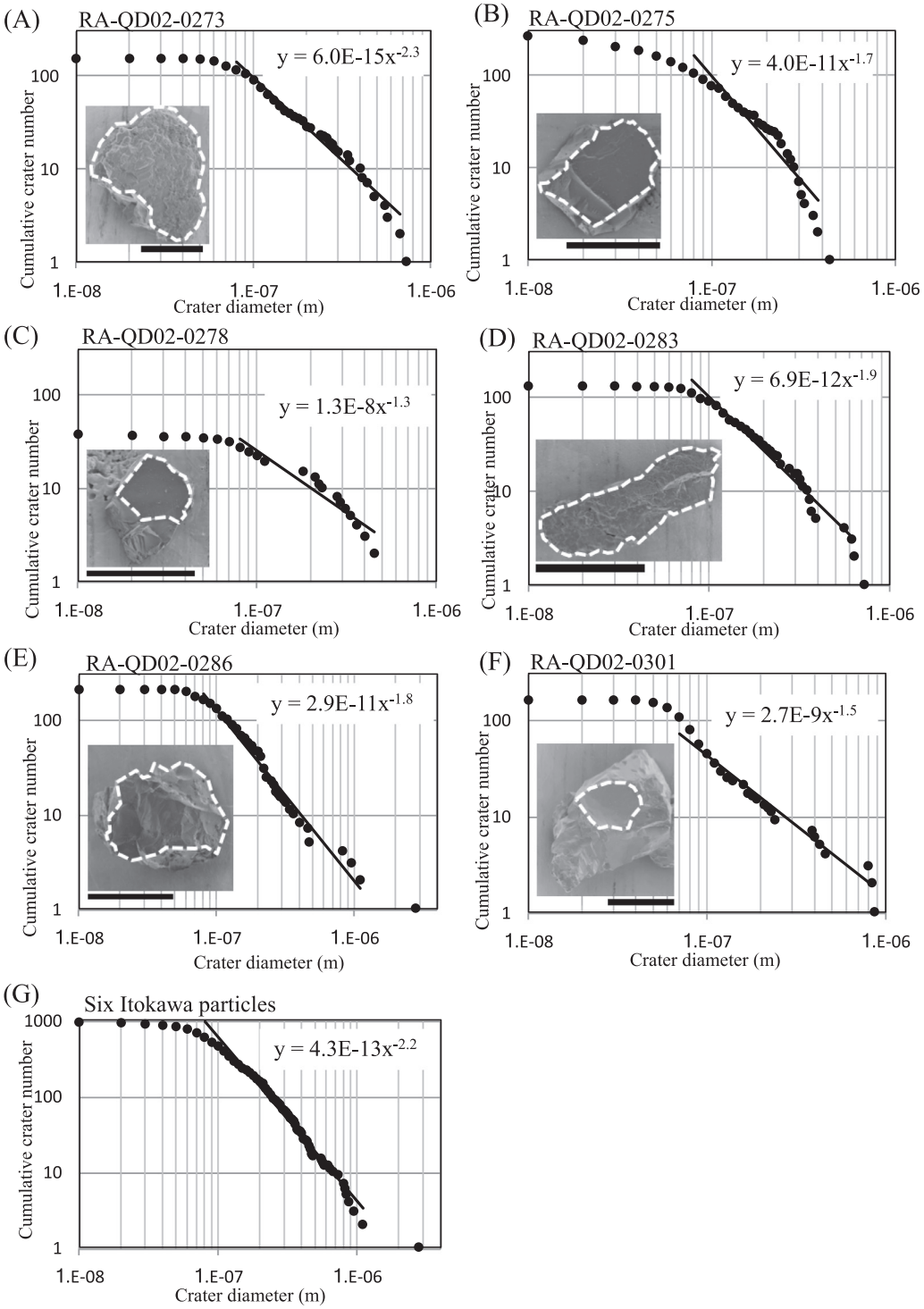

Fig. 5. Cumulative number of craters as a function of crater diameter (A–F) for six Itokawa particles, as well as (G) the combination of all craters on all six Itokawa particles. Best-fitting slopes and fitting functions are shown in the panels. The bottom left-hand images in each panel show SE images of the observed particles. The areas of investigation are surrounded by dashed lines in the SE images. Scale bars below the SE images correspond to 100 μm. Information on the investigated surfaces and investigation conditions are described in Table 2. Regarding RA-QD02-0273 and RA-QD02-0278, some craters within the investigated area may have been missed during counting because a lower magnification was used (× 4000 to × 10,000) than for the other samples (× 20,000) (Table. 2).

4. Discussion

4.1. Origin of submicrometer craters

We estimated the flux of the impactors responsible for the formation of submicrometer craters on Itokawa particles to constrain the formation process of these craters. Based on the best-fitting power-law slope to the total cumulative size distribution of 943 craters on six Itokawa particles (Fig. 5G), we calculated the cumulative distribution of the impactors, $N(m)$. We used experimental impact data from Hörz et al. (1975) to estimate the mass of the impactors based on the observed crater diameters,

$$D = cm^{\lambda}, \quad (1)$$

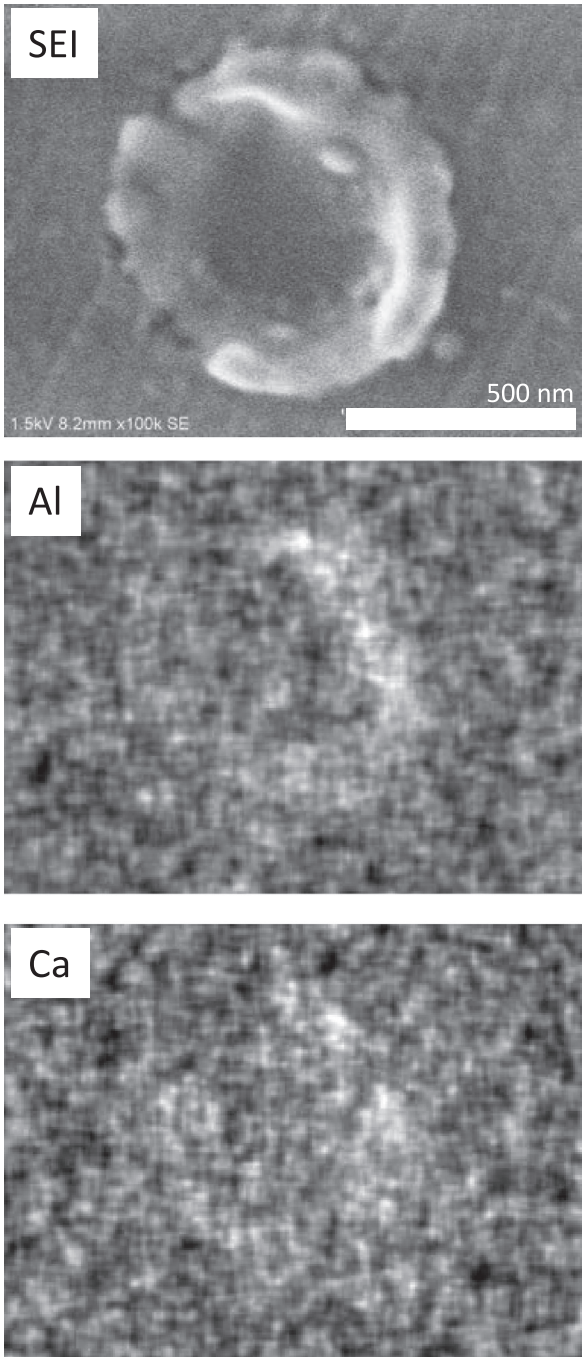

Fig. 6. (A) SE image of a crater on an olivine grain of RA-QD02-0275 and elemental abundance maps for Kα X-rays of (B) Al and (C) Ca.

where $c = 8.24$ and $\lambda = 0.37$, D is the crater diameter in centimeters, and m is impactor mass in grams. An impactor density of 3 g cm^{-3} and an impact speed of 20 km s^{-1} were assumed. The latter is the relative velocity between meteoroids at 1 AU (Zook, 1975). The ratio of crater diameter D to impactor diameter d (D/d) for spherical impactors varies from approximately 1.5 to 2 in the range from 10 nm to 1 µm, as estimated from Eq. (1). These D/d values are similar to the value of 1.60 ± 0.17 obtained by laboratory impact experiments using silica projectiles (0.48–2.40 µm in diameter) at an impact speed of ~6 km s^{-1} (Price et al., 2010), which represent simulations of dust impacts on Al foils of the Stardust spacecraft. Since D/d values for projectiles below 100 nm in diameter are poorly constrained by current impact experiments, we tentatively assume that Eq. (1) can be adapted to the smallest projectile sizes (10–100 nm). The cumulative impactor flux, $F(m)$, is calculated as

$$F(m) = \frac{N(m)}{ST}, \tag{2}$$

where the total investigated area of Itokawa particles, $S = 67{,}025$ µm^2 (Fig. 5). T is the time needed for craters to accumulate during direct exposure to the space environment. The common appearance of blisters on cratered surfaces (Figs. 1 and 2) indicates that cratered surfaces exposed to the Sun are subject to solar-wind accumulation. Previous investigations of the solar-flare track density showed that regolith particles spend up to of order 10^3 to 10^4 yr in the top few centimeters of Itokawa's surface (Keller and Berger, 2014; Noguchi et al., 2014), which yields an upper limit to T. Measurements of solar-wind noble gases indicate that Itokawa particles were directly exposed to the space environment for 150–550 yr (Nagao et al., 2011). Therefore, we assumed T in the range from 10^2 to 10^4 yr. We plotted $F(m)$ as a function of m in Fig. 7 for $T = 10^2$, 10^3, and 10^4 yr. We compared the impactor flux on Itokawa regolith with both the impactor flux on the lunar surface (Grün et al., 1985) and interplanetary dust flux models (Grün et al., 1985; Divine, 1993; Jehn, 2000). The interplanetary dust flux model was obtained by taking into account the dust flux measured by Pioneer 8 and 9 (Fig. 7), and calculation of the dust dynamics considered collisional effects, radiation pressure, and the Poynting–Robertson effect (Grün et al., 1985). We show the dust flux curves at 1 au and 1.7 au in Fig. 7, which roughly correspond to Itokawa's perihelion at 0.9530 AU and its aphelion at 1.6947 AU (Fujiwara et al., 2006). The interplanetary dust population along Itokawa's orbital path is probably contained within the two flux curves. The interplanetary dust flux model is in good agreement with dust detections at 1 AU by the Ulysses (Wehry and Mann, 1999) and STEREO spacecraft (Meyer-Vernet et al., 2009; Zaslavsky et al., 2012). Grün et al. (1985) also constructed the impact flux curve pertaining to the lunar surface (Fig. 7) using the crater size distribution of lunar rocks (Morrison and Zinner, 1977; Morrison and Clanton, 1979) and Eq. (1). They showed that the impact flux curve on the lunar surface is up to a factor of 100 higher than the interplanetary dust flux for particles with masses of $< 10^{-9}$ g. Independently, experiments pertaining to hypervelocity impacts under oblique impact angles (Flavill et al., 1978; Allison and McDonnell, 1982; Zook et al., 1984) imply that the lunar microcrater population below 7 µm crater diameter—corresponding to a mass of 10^{-11} g according to Eq. (1)—is probably dominated by cratering caused by secondary ejecta. Therefore, Grün et al. (1985) concluded that secondary ejecta particles contribute to the production of microcraters (particle mass $m < 10^{-9}$ g) on the lunar surface. Fig. 7 shows that the impactor flux on Itokawa particles is at least one order of magnitude higher than the interplanetary dust flux ($T = 10^4$ yr) and comparable to the case of the Moon ($T = 10^2$ to 10^3 yr). Considering that $T = 10^2$ to 10^3 yr is most likely the direct-exposure age according to the noble-gas analysis (Nagao et al., 2011), we conclude that secondary ejecta impacts are probably the dominant cratering process in the submicrometer-size range on Itokawa regolith particles, as well as on the lunar surface.

The surface of Itokawa is characterized by two regions (Fujiwara et al., 2006). The first region is rough and covered by boulders with sizes from a few to 50 m. The second region is smooth and rich in coarse, 1–5-cm-sized pebbles. The smooth and rough terrain might typically be characterized by centimeter- and meter-sized surface unevenness, respectively. This unevenness of the terrain might be accompanied by depressions, which have widths and depths comparable to the unevenness. Primary impacts by interplanetary dust in a depression can produce impact

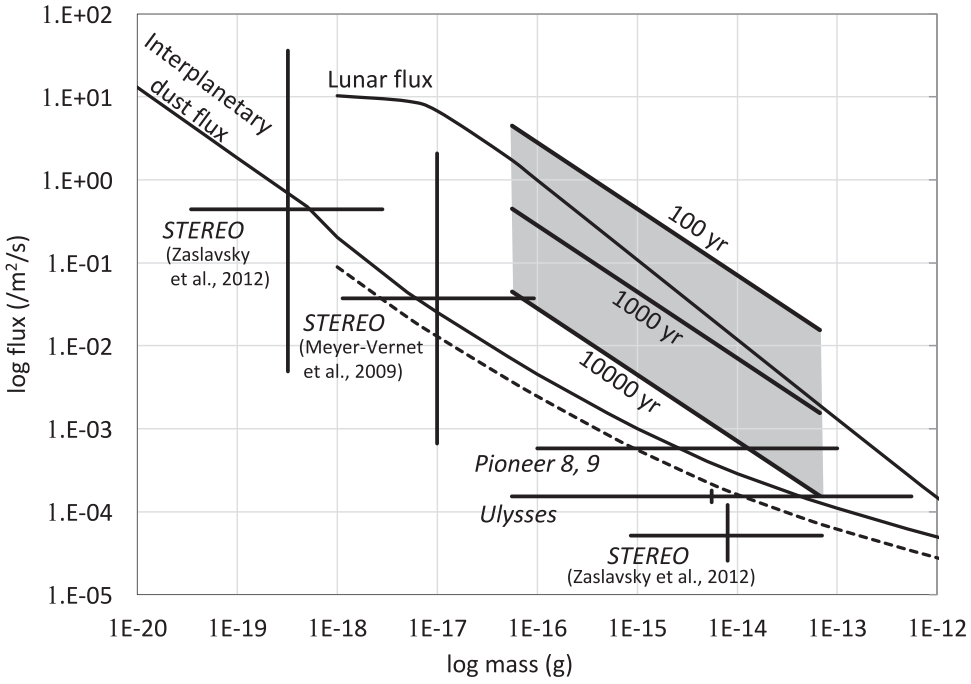

Fig. 7. Cumulative fluxes of impactors on six Itokawa particles estimated using the best-fitting slope from Fig. 5G. Estimated submicrometer impactor fluxes of the six Itokawa particles for $T = 10^2$, 10^3, and 10^4 yr (see the black lines labeled 100, 1000, and 10,000 yr, respectively). The range of estimated impactor fluxes for Itokawa particles is displayed as a gray parallelogram. Submicrometer impactor flux at the lunar surface (Gruñ et al., 1985): black solid line labeled lunar flux. Interplanetary dust flux models at 1 AU (Grün et al., 1985; Jehn, 2000) and 1.7 AU (Jehn, 2000): black solid line (1 AU) and black dashed line (1.7 AU). Results from dust detection by spacecraft at 1 AU: Pioneer 8 and 9 (Berg and Grün, 1973), Ulysses (Wehry and Mann, 1999), and STEREO (Meyer-Vernet et al., 2009; Zaslavsky et al., 2012); black uncertainty ranges.

ejecta, which can be blocked by nearby regolith or rocks and form secondary craters, provided that a primary impact crater is much smaller than the depression. We determined whether primary impacts can occur within depressions on Itokawa during the expected surface exposure time for regolith particles of 10^3 yr. Using the interplanetary dust flux model at 1 AU (Gruñ et al., 1985), we estimated the expected number of primary interplanetary dust impacts accumulated for 10^3 yr within areas ranging from 1 cm^2 to 1 m^2, which correspond to the expected size scale of the depressions in the smooth and rough terrain on Itokawa, respectively (Fig. 8). In Fig. 8, we plotted the cumulative impact number as a function of the mass of the interplanetary dust particles and the corresponding impact crater diameters calculated using Eq. (1). Fig. 8 shows that one or more primary craters smaller than 200 µm can be formed within an area of 1 cm^2 in 10^3 yr. Similarly, primary craters smaller than 6 mm can be produced within an area of 1 m^2 in 10^3 yr. In both cases, the maximum primary crater diameters of 200 µm and 6 mm are much smaller than the expected sizes of the depressions in the smooth and rough terrain of 1 cm^2 and 1 m^2, respectively. Hence, secondary ejecta that escaped from primary craters can be captured easily by the depression walls. Hypervelocity oblique impact experiments by Fravill and McDonnell (1977) and Fravill et al. (1978) showed that ejecta from primary impact craters with an average diameter of 14 µm produced numerous secondary submicrometer craters. In addition, Zook (1984) reported oblique impacts of milligram glass and basalt projectiles, which may produce millimeter-scale primary craters, creating numerous submicrometer craters. These experiments suggest that primary impact cratering with sizes larger than 10 µm can produce ejecta with sufficient velocity to result in submicrometer secondary cratering. We estimated the number of primary impacts that can produce secondary submicrometer craters, assuming that the formation of primary impact craters larger than 10 µm can lead to the production of submicrometer craters. Fig. 8 shows that 3×10^1 primary impact craters and 3×10^5 primary impact craters larger than roughly 10 µm can be produced within 1 cm^2 and 1 m^2, respectively. Oblique primary impact experiments indicated that the number of secondary craters is more than two orders of magnitude higher than those associated with primary im-

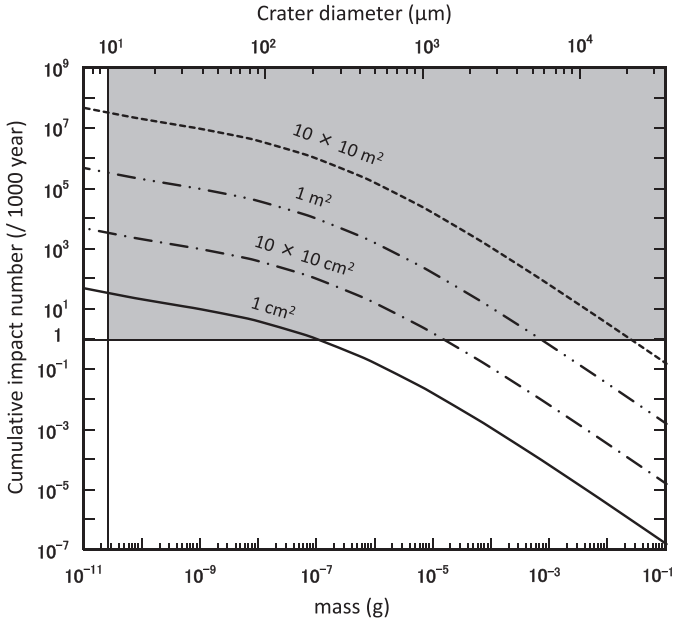

Fig. 8. Number of primary interplanetary dust impacts accumulated for 1000 yr within an area from 1 cm^2 to 10×10 m^2, calculated using the interplanetary dust flux at 1 au of Grün et al. (1985). The bottom horizontal axis shows the mass of the interplanetary dust. The top horizontal axis shows the crater diameter converted from the mass of interplanetary dust using Eq. (1) of Hörz et al. (1975). The gray area corresponds to the condition where one or more primary impacts occur with an impact crater diameter larger than 10 µm, which can produce submicrometer secondary craters.

pacts (Zook, 1984). Therefore, we conclude that secondary submicrometer craters can be formed during regolith exposure to primary impacts of interplanetary dust in the depressions of either smooth or rough terrain on Itokawa. Since global granular convection is expected to segregate and migrate regolith particles from rough to smooth terrain (Miyamoto et al., 2007), submicrometer cratering observed on Itokawa particles might have occurred in either smooth or rough terrain. If the surface unevenness of centimeter to meter scales is a significant factor driving the abundance of submicrometer secondary cratering, it is possible that the secondary particle flux can attain similar values among airless bodies, regardless of the overall shapes or sizes of those bodies, when the flux of the incident interplanetary dust particles is similar. This can explain the similar flux values for Itokawa and the Moon (Fig. 7).

4.2. Interpretation of crater morphology and spatial distribution

Craters without blisters (Fig. 2B) on the blistered surface of RA-QD02-0275 might have been formed after the initial blister formation period on the grain surface, while craters with blisters (Fig. 2C, D) dispersed on the same grain surface might have been generated prior to blister development. These features indicate that craters of various formation epochs may coexist on the same grain surface. The common appearance of craters without blisters suggests that most craters might have formed within a shorter time frame than the exposure time required for blister formation.

Elongation and partial disappearance of crater rims (Fig. 2A, D) are characteristic features of oblique impacts on micrometer scales (Wozniakiewicz et al., 2014). Elongation in the impact direction and the absence of crater rims on the incident side of the crater becomes apparent at impact angles greater than 15°–35° (Wozniakiewicz et al., 2014). Sub-micrometer-sized elongate and shallow craters were also identified on Al foils of the Stardust Intersteller Dust Collector. They are thought to have been formed by secondary ejecta through oblique impacts (Burchell et al., 2012; Stroud et al., 2014). The locally concentrated craters tend to exhibit oblique impact features (Fig. 2A); the top sections of crater rims are absent in Fig. 2A, which may provide an indication of the incident direction of the oblique impacts. The possible impactor trajectories of concentrated craters are displayed as arrows in Fig. 2A and Fig. 4B, based on considering the direction of crater elongation and the absence of crater rims. The trajectories originate from similar directions, suggesting that impactors from a common impact event were a major contributor to the locally concentrated crater distribution. Harries et al. (2016) identified 15 craters larger than 200 nm in diameter on a small Itokawa particle (RA-QD02-0265), corresponding to a crater number density of 0.08 μm^{-2}, which corresponds to the most heavily cratered surface previously reported. In this study, the number density of locally concentrated craters larger than 200 nm in size reaches 0.1 μm^{-2} across areas of approximately 40 μm^2 on RA-QD02-0272, while widely distributed craters larger than 200 nm have number densities of approximately 2.6×10^{-3} μm^{-2} to 4.5×10^{-3} μm^{-2}. The cratered surface reported by Harries et al. (2016) may correspond to concentrated crater areas on large Itokawa particles, such as those shown in Fig. 4B. Harries et al. (2016) proposed that the craters on RA-QD02-0265 were formed simultaneously by a nearby, small-scale impact. Our observations support the conclusion that locally concentrated craters were formed by projectiles from a single primary impact.

The melted drops and splashes that commonly coexist with craters could have been closely related to impact phenomena causing secondary craters. A low impact velocity (< 5 km s^{-1}) for the formation of the submicrometer craters on Itokawa particles was proposed by Harries et al. (2016) because of the craters' shallow depths and the absence of spallation zones. Dobrică and Ogliore (2016) calculated that micrometer-sized melt splashes on Itokawa particles could have been cooled and solidified for 200 μs (for 2 μm melted grains), based on considering radiative cooling. Assuming an ejecta velocity from the primary impact of less than 5 km s^{-1}, the melts might have been excavated within a distance of 1 m from the impact. This traveling distance is consistent with the idea that impactors of secondary craters were transported to centimeter- to meter-sized depressions.

The Ca- and Al-rich components detected in the craters are probably residues of the impactors, while craters indistinguishable from the host olivine surfaces on the basis of EDS mapping could have residues composed of the same elements as those of the host olivine. Since Ca and Al (and potentially Mg, O, Si, and Fe) in the residues are major elements of chondritic materials, corresponding to the composition of both Itokawa (Nakamura et al., 2011) and interplanetary dust, the crater residues may be either remnants of primary interplanetary dust impacts, as proposed by Harries et al. (2016), or Itokawa's own material.

Pulse laser irradiation experiments have been performed to simulate micro-impacts, because laser irradiation causes local heating to form nanometer-sized iron particles and reproduces the optical properties of space weathering on S-type asteroids and the Moon (Sasaki et al., 2001). Fazio et al. (2018) reported that a pulse laser shot produced crater-like morphologies on olivine surfaces and many cracks appeared at the laser spot. The cracks induced by pulse laser irradiation on various types of ceramics may be caused by thermal stress, solidification stress after melting of the surface layer, and/or volume changes owing to a solid–solid phase transition (Morita, 1993). Cracks in craters on troilite grains (Fig. 2E) could have been generated by processes similar to those causing the pulse laser-induced cracks through impact heating, followed by radiative cooling. Development of cracks only on troilite grains could reflect the different thermal properties of silicate and troilite.

4.3. Abundance of submicrometer craters

In the present study, craters were not identified on Itokawa particles smaller than 80 μm from either room A or room B. Thus far, craters have rarely been identified based on surface observations of small Itokawa particles (Matsumoto et al., 2016). To determine the particle size dependence of the crater population, we modeled the crater abundance on Itokawa particles larger than 80 μm and applied the model to predict crater abundances on smaller (< 80 μm) particles (details are provided in the Appendix). The crater abundance model assumed that 40% of Itokawa particles are surrounded by crater-rich surfaces with a crater density of 2.6×10^{-3} μm^{-2} for craters larger than 200 nm. This crater density corresponds to surfaces covered with widely dispersed craters. Craters larger than 200 nm can be clearly identified from surface observations. In the grain size histogram of the population of examined Itokawa particles smaller than 80 μm (Fig. 3), we show the expected number of particles that contain at least one crater larger than 200 nm in each bin of the size histogram. Fig. 3 also includes the grain size histogram resulting from previous observations (Nakamura et al., 2012; Harries et al., 2016; Matsumoto et al., 2016). From a re-examination of the SEM data obtained by Matsumoto et al. (2016), two 200-nm-sized crater candidates were identified on a 50-μm-sized particle (RA-QD02-0033) on which no craters had been noticed so far. This result has been added to Fig. 3. The crater abundance on the small Itokawa particles from room A is comparable to or slightly lower than that expected from the model for larger particles (> 80 μm), indicating that the size dependence of the crater abundance is not distinct for room A particles. The slightly lower abundance of craters on small Itokawa

particles ($< 80\,\mu m$) could have been caused by regolith fragmentation from larger to smaller particles through continuous meteorite bombardments (Tsuchiyama et al., 2011) or cyclic thermal fatigue (Delbo et al., 2014). The regolith fragmentation could have produced smaller particles with fresh surfaces during the time they were present on Itokawa, because the timescale of regolith fragmentation could have been shorter than that of blister formation ($< 10^3$ years; Matsumoto et al., 2016). Otherwise, small particles could have a tendency to escape from Itokawa, resulting in a loss of long-exposed particles. The crater abundance of room B particles is distinctively lower than the modeled abundance of the large Itokawa particles in room A. Note that a fraction of room B particles may have been crushed by an Al_2O_3 glass plate set in room B of the sample catcher for contamination monitoring (Yada et al., 2014). Therefore, we cannot conclude whether the low crater abundance of room B particles has preserved the original crater abundance or whether it was reduced by artificial fragmentation.

4.4. Implications

The common appearance of the submicrometer craters on Itokawa particles enables extensive future analysis. Further statistical studies of impact residues in submicrometer craters can restrict the chemical composition of the primary impactors, which in turn can provide insights into the origin of interplanetary dust. Harries et al. (2016) proposed that secondary submicrometer cratering can contribute to space weathering of asteroids. Because submicrometer cratering can occur anywhere on Itokawa, submicrometer cratering can promote space weathering on Itokawa globally. Further nanometer-scale observations of submicrometer craters are necessary to clarify the effectiveness of space weathering through secondary micro-impacts. The abundance of submicrometer craters on Itokawa particles implies ubiquitous generation of submicrometer impact ejecta. Although the majority of impact ejecta will escape to the space environment owing to Itokawa's low gravity, some will form impact craters and could be retained as levitating dust sustained by electric charge (e.g., Hartzell and Scheeres, 2013) and submicrometer ejecta dust clouds, which have been found on Jupiter's moons (Krüger et al., 1999) and are expected to surround all celestial bodies without atmospheres (Krüger et al., 2003). Studies of ejecta properties based on submicrometer craters will shed light on the dust behavior and evolution of airless bodies in micro-gravity.

5. Conclusion

Since cratering structures among Itokawa particles were previously considered rare, we studied numerous submicrometer-sized craters on Itokawa particles with sizes of up to 240 µm. The crater abundance does not vary significantly with particle size. Their morphologies are similar to those of craters of similar size on lunar regolith and fragments of carbonaceous chondrites. Craters produced during various formation epochs may coexist on the same grain surface. The estimated range of flux for craters on Itokawa particles is higher than the interplanetary dust flux and comparable to that for the submicrometer craters on lunar rocks. The higher flux at the lunar surface than the interplanetary flux was explained by high-speed secondary ejecta impacts and not by primary interplanetary dust impacts. Therefore, we conclude that secondary ejecta impacts are probably the dominant cratering process in the submicrometer-sized range on Itokawa regolith particles, as well as on the lunar surface. We demonstrated that secondary submicrometer craters can be produced anywhere in centimeter- to meter-sized depressions on Itokawa's surface by primary interplanetary dust impacts, while regolith particles remained on Itokawa. If the surface unevenness of centimeter to meter scales is an important factor driving the generation of submicrometer secondary cratering, hence irrespective of the overall shapes or sizes of celestial bodies, the similar flux values for Itokawa and the Moon can be explained.

Acknowledgments

We thank the Hayabusa project team for the sample return. We also appreciate the JAXA curation team for giving us an opportunity to study Itokawa particles and supporting our SEM observations at the JAXA curation facility. We are grateful to Dr. T. Hirai, Dr. A. Nakamura, Dr. M. Arakawa, and Dr. A. Tsuchiyama for helpful advice. This work was partly supported by the Nanotechnology Platform Program (Molecule and Material Synthesis) of the Ministry of Education, Culture, Sports, Science and Technology (MEXT), Japan and the Hypervelocity Impact Facility (formerly the Space Plasma Laboratory), ISAS, JAXA. The work of S.H was supported by JSPS KAKENHI Grants (Numbers JP15K05277 and JP17K05636).

Appendix

Modeling of the abundance of submicrometer craters on Itokawa particles

The abundance of craters on large Itokawa particles ($> 80\,\mu m$) is roughly modeled to predict the abundance of smaller Itokawa particles containing craters. The model is based on the abundance of crater-rich surfaces among Itokawa particles and the crater density of crater-rich surfaces. We divided the surface of Itokawa particles larger than 80 µm into segments of $20 \times 20\ \mu m^2$ and counted the number of segments on which craters were found. We found that approximately 40% of segments of particles larger than 80 µm include craters, implying that roughly 40% of surfaces were exposed to the space environment sufficiently long to accumulate secondary craters with suitable geometry. The number density of the widely dispersed craters is approximately $2.6 \times 10^{-3}\ \mu m^{-2}$ for craters larger than 200 nm. Such craters can be clearly recognized from surface observations. We adopted a model for the crater abundance on Itokawa particles that satisfied both conditions; 40% of Itokawa particles are covered by crater-rich surfaces on which craters were randomly dispersed with a crater density of $2.6 \times 10^{-3}\ \mu m^{-2}$. Using this model, we evaluated the expected fraction of Itokawa particles with average diameter D (µm), on which craters larger than 200 nm can be identified. When we investigated the surface of a particle of average diameter D (µm), the projected area $S = \pi D^2/4$ (μm^2) was regarded as our investigation area. For a crater-rich surface of area S with a crater density of $\rho = 2.6 \times 10^{-3}\ \mu m^{-2}$ the probability $p(a, S)$ that a craters are found in area S can be derived from the Poissonian distribution,

$$p(a,\ S) = \frac{S \times \rho^a}{a!} e^{-S\times\rho}. \tag{A.1}$$

We next obtained the probability $P(S)$ that at least one crater is found on a crater-rich surface of area S,

$$P(S) = 1 - [p(0, S)] = 1 - e^{-S\times\rho}. \tag{A.2}$$

A probability P of 90% is calculated for particles larger than 40 µm, while the probability is only 10% for particles of 10 µm in size. For our investigation of L Itokawa particles, 40% of the particles are assumed to have crater-rich surfaces. The number of Itokawa particles, N, that are composed of crater-rich surfaces, is expressed as $N = 0.4L$. To obtain the probability $Q(S, n, N)$ that at least one crater is located on each n Itokawa particles when L particles are investigated, a binomial distribution can be adopted,

$$Q(S, n, N) = {}_N C_n \left(1 - e^{-S\times\rho}\right)^n \left(e^{-S\times\rho}\right)^{N-n}. \tag{A.3}$$

We can now calculate the expectation value and the standard deviation of Q, which have the form,

$$E = N\left(1 - e^{-S\times\rho}\right); \tag{A.4}$$

$$\sigma^2 = N\left(1 - e^{-S\times\rho}\right)e^{-S\times\rho}. \tag{A.5}$$

Using Eqs. (A.4) and (A.5), we can estimate the expected number of Itokawa particles that have at least one crater larger than 200 nm in each bin of the size histogram of Fig. 3. We estimated E and σ for a set of Itokawa particles belonging to each bin smaller than 80 μm, where L is the number of Itokawa particles in the same bin. To simplify the estimation, the particle diameter D was assumed to be equal to the mean D of all particles in the same bin. The calculated E and σ values are included in Fig. 3.

References

Allison, R.J., McDonnell, J.A.M., 1982. Secondary cratering effects on lunar microterrain-Implications for the micrometeoroid flux. In: Lunar and Planetary Science Conference XII, pp. 1703–1716.

Bonal, L., et al., 2015. Visible-IR and Raman microspectroscopic investigation of three Itokawa particles collected by Hayabusa: mineralogy and degree of space weathering based on nondestructive analyses. Meteorit. Planet. Sci. 50 (9), 1562–1576.

Brownlee, D.E., et al., 1973. Morphology of micron sized impact craters on lunar glasses. In: Lunar and Planetary Science Conference IV, pp. 97–99. Abstracts.

Brownlee, D.E., Rajan, R.S., 1973. Micrometeorite craters discovered on chondrulelike objects from Kapoeta meteorite. Science 182, 1341–1344.

Burchell, M.J., et al., 2012. Experimental investigation of impacts by solar cell secondary ejecta on silica aerogel and aluminium foil: implications for the stardust interstellar dust collector. Meteorit. Planet. Sci. 47, 671–683.

Clark B.E., et al., 2002. Asteroid Space Weathering and Regolith Evolution. In Asteroid III (eds. W. Bottke Jr., A. Cellino, P. Paolicchi and R. P. Binzel) The Univ. of Arizona Press, Tucson (AZ). pp. 585–599.

Delbo, M., et al., 2014. Thermal fatigue as the origin of regolith on small asteroids. Nature 508, 233–236.

Divine, N., 1993. Five populations of interplanetary meteoroids. J. Geophys. Res. 98, 17029–17048.

Dobrică, E., Ogliore, R.C., 2016. Adhering grains and surface features on two Itokawa particles. Earth, Planets Space 68 (1), 21.

Fazio, A., et al., 2018. Femtosecond laser irradiation of olivine single crystals: experimental simulation of space weathering. Icarus 299, 240–252.

Fechtig, H., et al., 1974. Lunar microcrater studies, derived meteoroid fluxes, and comparison with satellite-borne experiments. In: Proceedings of the Lunar and Planetary Science Conference V, pp. 2463–2474.

Flavill, R.P., et al., 1978. Primary, secondary and tertiary microcrater populations on lunar rocks effects of hypervelocity impact microejecta on primary populations. In: Proceedings of the Lunar and Planetary Science Conference IX, pp. 2539–2556.

Flavill, R.P., McConnell, J.A.M., 1977. Laboratory simulation of secondary lunar microcraters from micron scale hypervelocity impacts on lunar rock. Meteoritics 12, 220.

Fujiwara, A., et al., 2006. The rubble-pile asteroid Itokawa as observed by Hayabusa. Science 312, 1330–1334.

Gruň, E., et al., 1985. Collisional balance of the meteoritic complex. Icarus 62, 244–272.

Goswami, J.N., et al., 1976. Microcraters and solar flare tracks in crystals from carbonaceous chondrites and lunar breccias. In: Proceedings of the Lunar and Planetary Science Conference VII, pp. 543–562.

Harries, D., et al., 2016. Secondary submicrometer impact cratering on the surface of asteroid 25143 Itokawa. Earth Planet. Sci. Lett. 450, 337–345.

Harries, D., Langenhorst, F., 2014. The mineralogy and space weathering of a regolith grain from 25143 Itokawa and the possibility of annealed solar wind damage. Earth Planets Space 66, 163.

Hartzell, C.M., Scheeres, D.J., 2013. Dynamics of levitating dust particles near asteroids and the Moon. J. Geophys. Res.: Planets 118, 116–125.

Hörz, F., et al., 1975. Lunar microcraters: implications for the micrometeoroid complex. Planet. Space Sci. 23, 151–172.

Jehn, R., 2000. An analytical model to predict the particle flux on spacecraft in the solar system. Planet. Space Sci. 48, 1429–1435.

Keller, L.P., Berger, E.L., 2014. A transmission electron microscope study of Itokawa regolith grains. Earth, Planets Space 66, 71–77.

Krüger, H., et al., 1999. Detection of an impact- generated dust cloud around Ganymede. Nature 399, 558–560.

Krüger, H., et al., 2003. Impact-generated dust clouds surrounding the Galilean moons. Icarus 164, 170–187.

Langenhorst, et al., 2014. Mineralogy and defect microstructure of an olivine-dominated Itokawa dust particle: evidence for shock metamorphism, collisional fragmentation, and LL chondrite origin. Earth, Planets and Space, 66, p. 118.

Morita, N., 1993. Generation and propagation behavior of laser induced thermal cracks. J. Ceram. Soc. Jpn. 101, 527–552.

Matsumoto, T., et al., 2016. Nanomorphology of Itokawa regolith particles: application to space-weathering processes affecting the Itokawa asteroid. Geochim. Cosmochim. Acta 187, 195–217.

Matsumoto, T., et al., 2015. Surface and internal structures of a space-weathered rim of an Itokawa regolith particle. Icarus 257, 230–238.

Melosh, H.J., 1989. Impact Cratering: A Geologic Process. (Oxford Monographs on Geology and Geophysics). Oxford University Press, New York.

Meyer-Vernet, N.M., et al., 2009. Dust detection by the wave instrument on stereo: nanoparticles picked up by the solar wind? Sol. Phys 256, 463–474.

Miyamoto, H., et al., 2007. Regolith migration and sorting on asteroid Itokawa. Science 316, 1011–1014.

Morrison, D.A., Clanton, U.S., 1979. Properties of microcraters and cosmic dust of less than 1000 A dimensions. In: Proceedings of the Lunar and Planetary Science Conference X, pp. 1649–1663.

Morrison, D.A., Zinner, E., 1977. 12054 and 76215 – new measurements of interplanetary dust and solar flare fluxes. In: Proceedings of the Lunar and Planetary Science Conference VIII, pp. 841–863.

Nagao, K., et al., 2011. Irradiation history of Itokawa regolith material deduced from noble gases in the Hayabusa samples. Science 333, 1128–1131.

Nakamura, T., et al., 2011. Itokawa dust particles: a direct link between S-type asteroids and ordinary chondrites. Science 333, 1113–1116.

Nakamura, E., et al., 2012. Space environment of an asteroid preserved on micrograins returned by the Hayabusa spacecraft. Proc. Natl. Acad. Sci. USA 109, E624–E629.

Nakashima, D., et al., 2013. Oxygen three-isotope ratios of silicate particles returned from asteroid Itokawa by the Hayabusa spacecraft: a strong link with equilibrated LL chondrites. Earth Planet. Sci. Lett. 379, 127–136.

Noguchi, T., et al., 2014. Space weathered rims found on the surfaces of the Itokawa dust particles. Meteorit. Planet. Sci. 49, 188–214.

Noguchi, T., et al., 2011. Incipient space weathering observed on the surface of Itokawa dust particles. Science 333, 1121–1125.

Price, M., et al., 2010. Comet 81P/Wild 2: the size distribution of finer (sub-10lm) dust collected by the Stardust spacecraft. Meteorit. Planet. Sci. 45, 1409–1428.

Robinson, M.S., et al., 2001. The nature of ponded deposits on Eros. Nature 413 (6854), 396–400.

Sasaki, S., et al., 2001. Production of iron nanoparticles by laser irradiation in a simulation of lunar-like space weathering. Nature 410, 555–557.

Schneider, E., et al., 1973. Microcraters on Apollo 15 and 16 samples and corresponding cosmic dust fluxes. In: Proceedings of the Lunar and Planetary Science Conference IV, pp. 3277–3290.

Stroud, et al., 2014. Stardust Interstellar Preliminary examination XI: identification and elemental analysis of impact craters on Al foils from the Stardust interstellar dust collector. Meteorit. Planet. Sci. 49, 1698–1719.

Thompson, M.S., et al., 2014. Microchemical and structural evidence for space weathering in soils from asteroid Itokawa. Earth, Planets Space 66 (1), 1–10.

Tsuchiyama, A., et al., 2011. Three dimensional structure of hayabusa samples: origin and evolution of itokawa regolith. Science 333 (6046), 1125–1128.

Turcotte, D.L., 1986. Fractals and fragmentation. J. Geophys. Res. 91, 1921–1926.

Veverka, J., et al., 2001. The landing of the NEAR-Shoemaker spacecraft on asteroid 433 Eros. Nature 413, 390–393.

Wehry, A., Mann, I., 1999. Identification of beta-meteoroids from measurements of the dust detector onboard the ULYSSES spacecraft. Astron. Astrophys. 341, 296–303.

Wozniakiewicz, P.J., et al., 2014. Micron-scale hypervelocity impact craters: dependence of crater ellipticity and rim morphology on impact trajectory, projectile size, velocity, and shape. Meteorit. Planet. Sci. 1947 (10), 1929–1947.

Yada, T., et al., 2014. Hayabusa-returned sample curation in the planetary material sample curation facility of JAXA. Meteorit. Planet. Sci. 49 (2), 135–153.

Yano, H., et al., 2006. Touchdown of the Hayabusa spacecraft at the Muses Sea on Itokawa. Science 312, 1350–1353.

Yurimoto, H., et al., 2011. Oxygen isotopic compositions of asteroidal materials returned from Itokawa by the Hayabusa mission. Science 333, 1116–1119.

Zaslavsky, A., et al., 2012. Interplanetary dust detection by radio antennas: mass calibration and fluxes measured by STEREO/WAVES. J. Geophys. Res.: Space Phys. 117 (A5), A05102.

Zook, 1975. the state of meteoritic material on the moon. In: Proceedings of the 6th Lunar Science Conference, pp. 1653–1672.

Zook, H.A., et al., 1984. Lunar primary and secondary microcraters and the micrometeoroid flux. Lunar Planet. Sci. XV, 965–966.